A new convective instability of the rotating-disk boundary layer with growth normal to the disk

By J. J. H E A L E Y

Department of Mathematics, Keele University, Keele, Staffs ST5 5BG, UK
j.j.healey@keele.ac.uk

In this paper we extend the familiar concept of spatial instability and growth of disturbances in the downstream direction to include spatial instability and growth in the wall-normal direction. The stability theory of boundary layers has generally been concerned with determining the evolution of disturbances inside a boundary layer (this is where disturbances have their largest amplitudes and can cause a laminar boundary layer to become turbulent). Outside a boundary layer, where the basic flow is uniform, normal-mode disturbances decay exponentially with distance from the wall to satisfy homogeneous boundary conditions. In this paper we present a surprising scenario where an impulsive disturbance, made up of a superposition of these normal modes, nonetheless grows exponentially with distance from the wall. While the usual convective instability with exponential growth in the downstream direction can be efficiently characterized by spatial modes with complex wavenumbers, the new convective instability can be efficiently characterized by modes with exponentially diverging 'eigenfunctions' obtained by moving certain branch-cuts in the complex wavenumber plane. The new instability is therefore associated with an interaction between the discrete spectrum and the continuous spectrum. We emphasize, however, that the homogeneous boundary conditions are always satisfied, and that at any finite time exponential growth only occurs over a finite distance from the wall, but this distance increases linearly with time. Interactions between poles and branch-cuts have been found before, but the results presented here provide a physical interpretation for this spectral behaviour. A further curiosity is that some of these divergent modes have been found to violate Howard's semi-circle theorem.

1. Introduction

In this paper we consider linearized disturbances to a boundary layer. In particular, and somewhat unusually, we focus attention on those parts of the disturbances that extend outside of the boundary layer. This is the part of the disturbance solution to which the outer homogeneous boundary conditions are applied in order to obtain the dispersion relation. A simple calculation, shown below, then shows that outside the shear layer, where the basic flow is essentially uniform, normal modes decay exponentially with distance from the wall, seemingly indicating that no interesting behaviour should be expected outside the boundary layer.

However, we present here an example where an impulsive initial condition excites a superposition of normal modes whose collective behaviour produces a wavepacket that propagates in the wall-normal direction and grows exponentially in the wall-normal direction. This appears to be paradoxical because there is no source of energy

outside the boundary layer (the Reynolds stress is proportional to the mean shear, and is therefore zero outside the boundary layer) to sustain this growth. It is shown that the mechanism for producing this growth can be understood by considering the complete evolution of the disturbance in both downstream and wall-normal directions. This anomalous behaviour persists until the wavepacket has propagated a distance comparable to the length scale over which the basic flow is evolving, and so can be made arbitrarily large by increasing the Reynolds number (provided that a laminar basic flow is maintained). The behaviour has been found in an inviscid stability problem, and will also exist when viscosity is included.

Although our example involves a boundary-layer basic flow, the new behaviour could, in principle, arise whenever the basic flow can be considered unbounded in the direction normal to the direction of the flow in the shear layer, e.g. free shear layers, plane and circular wakes and jets etc. Indeed, as discussed in the conclusions, §6 below, there is evidence that growth may occur outside of some of these flows as well.

The stability equations for disturbances to parallel shear layers are routinely derived in textbooks on hydrodynamic stability theory, e.g. Lin (1955), Chandrasekhar (1961), Drazin & Reid (1981), Schmid & Henningson (2001), Drazin (2002), etc. In the inviscid two-dimensional version of the problem, the flow is often expressed as a sum of the prescribed basic flow in the x-direction, $U(y)$, where y is in the direction normal to the flow, and a small-amplitude unsteady component for the disturbance. The governing equations are then linearized in the disturbance quantities. The evolution of the disturbance from some given initial-value boundary-value problem can then be found by decomposing the disturbance into a superposition of modes proportional to $v(y) \exp \mathrm{i}(\alpha x - \omega t)$, where v is the component of the disturbance velocity in the y-direction, t is time, α is the streamwise wavenumber and ω is the angular frequency. These modes are then found to satisfy the Rayleigh equation

$$(U - c)(v'' - \alpha^2 v) - U'' v = 0 \tag{1.1}$$

where $c = \omega/\alpha$. The solution to the initial-value boundary-value problem can be realized in practice by taking appropriate inverse Fourier transforms, see, e.g., (2.11) below.

We shall refer to any modes that satisfy homogeneous boundary conditions as normal modes, or the discrete sprectrum. For a boundary layer adjacent to a plate at $y = 0$, these boundary conditions are $v(0) = 0$ and $\lim_{y \to \infty} v(y) = 0$. However, if there are branch-cuts in the transform planes, then these will contribute continuous spectra to the solution as well. Boundary layers, and other unbounded flows in the y-direction, have only a finite number of normal modes (and often only one unstable normal mode) and the continuous spectra are particularly important in describing the solution near the disturbance source. In these flows a continuous spectrum arises from the behaviour of v for large y, where $U \to$ const. and $U'' \to 0$, which reduces (1.1) to

$$v'' - \alpha^2 v = 0, \tag{1.2}$$

provided $\lim_{y \to \infty} U(y) \neq c$, with general solution

$$v = C_1 \exp(-\sqrt{\alpha^2} y) + C_2 \exp(\sqrt{\alpha^2} y). \tag{1.3}$$

We shall take the square-root symbol to denote the root with positive real part. This choice of square-root means that homogeneous boundary conditions are satisfied

when $C_2 = 0$, and it means that the branch-cuts for the square-root are placed along the imaginary axes of the complex α-plane.

Note that for inviscid problems there is a second continuous spectrum associated with branch-cuts emanating from the logarithmic singularity at critical points, y_c, where $U(y_c) = c$. Discussion of these branch-cuts will be deferred until later; our primary interest here lies in the branch-cuts associated with the decay of solutions as $y \to \infty$.

The contours of integration in the inverse Fourier transform can be placed along the real wavenumber axis provided that the contour in the complex frequency plane lies above all singularities in the frequency plane so that the principle of causality is observed. If there are no branch-cuts associated with decay as $y \to \infty$ (e.g. in a flow of finite extent in the y-direction), the integration contours in the complex wavenumber plane can be closed by introducing semi-circular arcs of large radius, and evaluated using Cauchy's residue theorem. The solution will then be a superposition of the normal modes produced by poles in the integrand. However, if there are branch-cuts along the imaginary wavenumber axes, then the contours cannot cross them, and so the large semi-circular arcs must be deformed to run down and around the imaginary axes, see figure 1(a), for example. The contribution to the inverse transform from the sides of the branch-cuts represents the continuous spectrum. The continuous spectrum describes the disturbance close to its source (the 'near field'); the discrete spectrum (if it exists, and is not heavily damped) describes the normal-mode behaviour of the disturbance far from the source (the 'far field'). Contours closed in the upper half-plane give the physical solution downstream of the source; contours closed in the lower half-plane give the physical solution upstream of the source.

In principle, unstable disturbances can always be described using the configuration shown in figure 1(a), where the wavenumber is real (the contour runs along the real axis), and the frequency is complex. This is called a temporal stability analysis. However, for some flows, it is possible to lower the contour in the frequency plane to (or just below) the real axis, while simultaneously deforming the contour in the wavenumber plane away from the real axis, as in figure 1(b), to prevent any poles from crossing the integration contour. If a pole crosses from the upper to the lower half-plane, as in the figure, then it corresponds to a normal mode that grows exponentially in the downstream direction. This representation of the disturbance using a real frequency and complex wavenumber is called a spatial stability analysis, and is useful in describing experiments involving periodically forced disturbances. This transformation of a temporal mode into a spatial mode, and a relation between the growth rates of the two, was given by Gaster (1962) for small growth rates, while Briggs (1964) describes the procedure in terms of a simultaneous deformation of integration contours that can be used for growth rates of arbitrary magnitude.

If the deformation can be accomplished, as in figure 1(b), then the flow is called convectively unstable and a disturbance with real frequency can grow exponentially with downstream distance, like that calculated by Gaster (1965). However, as shown in Briggs (1964), the deformation must be halted if a pole from one half-plane coalesces with a pole from the other half-plane before the imaginary part of the frequency has reached zero. In this case, the integration contour becomes 'pinched' between the poles, neither of which it can cross. There is then growth in time as well as space, and the flow is called absolutely unstable. The pinch point is in fact a saddle point of the integrand, and Gaster (1968) independently discovered the distinction between convective and absolute instability using a saddle-point theory. Briggs' pinch-point
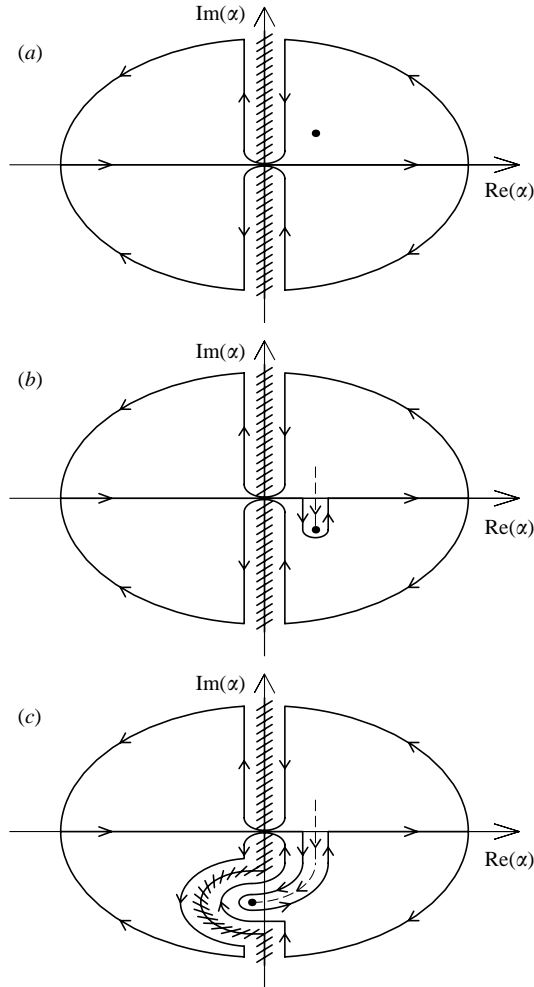
FIGURE 1. Examples of positions of poles (disks) giving normal modes for a given frequency, branch-cuts (hatched lines) giving the continuous spectrum and possible contours of integration (solid lines with arrows) in the complex wavenumber plane. Dashed lines indicate paths taken by poles as the imaginary part of the frequency is reduced to zero in the complex frequency plane. The contours can be closed in the upper half-plane when $x > 0$, and in the lower half-plane when $x < 0$.

method corresponds to checking that the integration contour lies within the valleys of the saddle point for the rest frame.

However, the present paper is concerned with another scenario, one in which, as the imaginary part of the frequency is reduced towards zero, a pole first crosses the real axis of the complex wavenumber plane, as in figure 1(b), but then goes on to cross the imaginary axis as well, as in figure 1(c). The integration contour must remain on the same side of the pole, and yet also cannot cross the branch-cut, so the branch-cut must be moved to accommodate the pole and contour, as suggested by Bers (1983) in a plasma physics context. However, Bers gives no actual example of this behaviour in the wavenumber plane, nor does he discuss what, if any, physical consequences

there might be (the branch-cut he considered arose directly from the model equations, rather than as part of the solution as in (1.3)).

Furthermore, there seem at first sight to be strong physical arguments against moving the branch-cuts. Moving a branch-cut away from the imaginary axis corresponds to switching to the exponentially diverging solution to (1.2), i.e. taking $C_1 = 0$ and $C_2 \neq 0$ in (1.3). Clearly, this solution fails to satisfy homogeneous boundary conditions, but this objection can be overcome by recognizing that a normal-mode solution only emerges as a far-field approximation to the solution of the initial-value problem; the normal mode does not appear instantaneously over an infinitely large domain. The solution is only required at finite times after the introduction of the disturbance, and at finite times the disturbance has only propagated a finite distance in the wall-normal direction. Beyond this finite distance, the undisturbed flow continues to satisfy homogeneous boundary conditions.

This picture of exponential growth over a certain wall-normal distance, followed by decay, resembles the behaviour of certain 'leaky waves' that can arise over a fluid-loaded elastic plate, see Crighton (1989). There is a uniform flow over the plate, and the plate is subject to periodic forcing at a point. Waves propagating in the plate downstream from the source are attenuated exponentially with downstream distance by radiating acoustic waves into the stream. The wave intensity in the stream is then found to increase exponentially with wall-normal distance into the stream. This is because the waves encountered further from the wall were excited further upstream where the wave in the plate was larger. However, this wall-normal growth eventually terminates when the Mach-cone (or Mach-wedge) for the source is reached, i.e. when those waves excited at the point forcing are reached, which are the largest waves in the system. Beyond the Mach-cone, a quiet zone is encountered, and there is decay in the wave intensity.

However, there are also significant differences between the behaviour of the disturbances associated with figure 1(*c*) and the behaviour of the leaky waves just described. The finite wall-normal distance over which the leaky waves grow is proportional to the downstream distance from the source, but for the waves of figure 1(*c*) this distance increases, in principle indefinitely, in proportion to time. This growth in the wall-normal direction suggests we are dealing with a new type of convective instability since the disturbance can propagate arbitrarily far from the source, and grow arbitrarily large in the process. This in turn raises the question of where the energy comes from in order to drive and sustain this instability. In a conventional convective instability where the disturbance propagates downstream through the boundary layer, it gains energy from the basic shear via the Reynolds stress terms as it propagates. However, outside the boundary layer there is no basic shear, and hence no source of energy. Nonetheless, as with the leaky waves, we shall show that the growth in the new convective instability can be understood by considering the propagation in both streamwise and wall-normal directions together.

This work was motivated by a recent asymptotic long-wave inviscid stability theory for the rotating-disk boundary layer, see Healey (2006), which predicted that the dominant saddle point (pinch point) becomes asymptotically close to the imaginary axis of the complex wavenumber plane as wavelengths increase. It also predicted that spatial branches (loci of poles as the real part of the frequency is varied) close to the saddle point cross the imaginary axis, like in figure 1(*c*).

In §2 we discuss the physical problem, present the linearized stability equations (a three-dimensional version of the Rayleigh equation (1.1)) and express the solution to the initial-value problem in terms of inverse Fourier transforms. In §3 numerical

solutions of the Rayleigh equation are used to show how the pinch-point solutions first found for this problem by Lingwood (1995) approach one of the branch-cuts, and that for long enough waves the spatial branches do indeed cross the imaginary axis as predicted by Healey (2006). These numerical calculations locating the dominant saddle point (pinch point) require a global investigation of the dispersion relation, which was not possible using the long-wave theory.

In §4 we extend the saddle-point method for calculating wavepacket propagation in boundary layers so that it can also be used to calculate propagation and growth in the wall-normal direction. These saddle points are found to cross the imaginary axis and have divergent eigenfunctions. The source of energy for this growth is also investigated in this section by mapping out the disturbance in both the streamwise and wall-normal directions. In §5 the wall-normal growth predicted by the divergent saddles is then compared with numerical integrations of the inverse Fourier transforms for an impulsive disturbance where the integration paths are chosen such that the eigenfunctions all decay in the wall-normal direction. Conclusions, and examples of other flows where this behaviour could appear, are given in §6.

2. Inviscid stability of the rotating-disk boundary layer

When an infinite disk rotates about its axis of symmetry in an otherwise still fluid, viscous stresses at the disk surface drag fluid elements near the disk around in almost circular paths, and centrifugal forces then cause these elements to spiral outwards. The disk thus acts as a centrifugal fan with a radial flow component that has a wall-jet character directed away from the axis of rotation. The fluid thrown outwards in this way is replaced by an axial flow towards the disk surface. The azimuthal flow component has a typical boundary layer profile, increasing monotonically from zero at the disk wall to a constant value proportional to the angular velocity of the disk and the distance to the axis of rotation (when considered, as here, in a frame of reference rotating with the disk). This basic flow is calculated using Kármán's (1921) similarity solution.

The importance of the cross-flow structure to the flow's stability was first recognized by Gregory, Stuart & Walker (1955) who observed a set of stationary vortices in an experimental study, and explained their appearance in terms of an inviscid inflectional 'cross-flow' instability. This cross-flow instability generates stationary vortices in many three-dimensional boundary layers of engineering interest, and they are believed to be involved in the laminar–turbulent transition process in many of these flows. Experiments on the rotating-disk boundary layer show that the stationary vortices are generated by points of surface roughness and grow in the direction of increasing radius, thus corresponding to a convective instability.

However, Lingwood (1995) showed that this flow becomes absolutely unstable to travelling waves far enough from the axis of rotation. Lingwood's location for convective–absolute transition coincides closely with the location of laminar–turbulent transition measured in many experimental studies, an observation that has generated much interest. Moreover, Lingwood found that the absolute instability exists in the inviscid limit. Healey (2004) used this inviscid result as the leading-order term in a large-Reynolds-number asymptotic expansion for the upper branch of the neutral curve for absolute instability in order to determine the effect of non-parallel terms on the absolute instability in this part of parameter space (they are found to be destabilizing). There are known to be at least two families of saddle points in the viscous problem and it was also found by Healey that Lingwood's saddle points only

form pinch points on the upper branch of the neutral curve for absolute instability below a certain finite Reynolds number, and it is a second family of saddle points that give the dominant saddles that asymptote towards the inviscid results as the Reynolds number increases. Lingwood's saddle points, however, do appear to be pinch points at large Reynolds numbers along the lower branch of the neutral curve, where the wavelengths increase as the Reynolds number increases.

This motivated Healey (2006) to develop an inviscid long-wave asymptotic theory for the absolute instability, as a starting point for a large-Reynolds-number asymptotic long-wave viscous theory for the lower branch of the neutral curve (Turkyilmazoglu & Gajjar (2001) independently derived an inviscid long-wave theory as well, but their solution is less complete). Healey's (2006) theory revealed several new fundamental features of the absolute instability in the long-wave limit. First, the absolutely unstable waves are dominated by the radial wall-jet component of the basic flow profile, except outside the boundary layer, where a small azimuthal cross-flow dominates (the radial component is exponentially small outside the boundary layer). Secondly, although the appropriately resolved component of the basic flow is inflectional, the critical points do not make the most significant contribution to the growth rate of the absolute instability. Thirdly, there are eight saddle points that coalesce as the azimuthal wavenumber tends to zero, one of which has exponentially diverging eigenfunctions, and another of which is the pinch point. The existence of so many saddles means care must be taken in determining which one is the pinch point as parameters in the problem are varied. It is the imaginary terms arising from the interaction of the saddles with each other that generate the dominant contribution to the instability mechanism (analogous to the inviscid instability mechanism of modal interaction). However, it is a fourth finding that motivates the present investigation, which is that the pinch point approaches the imaginary axis of the radial wavenumber plane as wavelengths increase, leading to modes crossing the imaginary axis as in figure 1(*c*). The purpose of this paper is to investigate in detail the physical consequences of this behaviour of the pinch point.

As first described by Gregory *et al.* (1955), and in many subsequent studies, e.g. Healey (2006), the inviscid linearized stability problem for the rotating disk can be reduced to the Rayleigh equation. We only give a brief summary of the main steps here. Let the disk rotate at constant angular velocity Ω_* in an otherwise still viscous incompressible fluid of kinematic viscosity ν_*. Lengths are then made dimensionless with the characteristic viscous length scale $(\nu_*/\Omega_*)^{1/2}$, which is the thickness of the boundary layer that forms over the disk, and time with Ω_*^{-1}. The flow field is expanded as the sum of the Kármán (1921) similarity solution for the basic flow and a small-amplitude disturbance (which does not take the same similarity structure). These expressions are substituted into the governing equations for viscous incompressible flow in cylindrical coordinates rotating with the disk, and linearized in disturbance quantities.

The disturbances are found to satisfy a set of linear partial differential equations that can be reduced to ordinary differential equations far from the axis of rotation. Therefore, let R_* be the dimensional radius of the position of interest on the disk, then a Reynolds number, Re, can be introduced that is the ratio of R_* to the boundary layer thickness:

$$Re = R_* \left(\frac{\Omega_*}{\nu_*} \right)^{1/2}. \qquad (2.1)$$

A new radial coordinate, ρ, is introduced,

$$r = Re\,\rho, \tag{2.2}$$

where r is the radius scaled by boundary layer thickness; $Re \gg 1$ and $\rho = O(1)$ near the position of interest. If $Re\,\alpha \gg 1$, where α is the radial wavenumber, then the radial wavelength is small compared with the distance to the axis of rotation, and the basic flow does not vary significantly on the length scales associated with the disturbance. This separation between the length scale of disturbance evolution and the length scale of basic flow evolution allows a WKB formulation to be adopted for the disturbance structure, in which disturbance quantities like, e.g., the axial velocity component $\hat{w}$, are written in the form

$$\hat{w}(r, \theta, z, t) = w(\rho, z)\exp \mathrm{i}Re\left(\int \alpha(\rho)\,\mathrm{d}\rho + \beta\theta - \omega t\right) \tag{2.3}$$

where (r, θ, z) are the dimensionless cylindrical coordinates (with the usual notation), t is dimensionless time and the azimuthal wavenumber $Re\,\beta$ is an integer. We assume $Re\,\beta \gg 1$ and so will neglect the discretization of the scaled azimuthal wavenumber β, which is discretized in units of Re^{-1}. The dimensionless angular frequency of the disturbance, ω, is the dimensional frequency divided by $Re\,\Omega_*$. Substituting (2.3), and expressions like it for the other disturbance quantities, into the linearized disturbance equations and neglecting terms of $O(Re^{-1})$ gives ordinary differential equations for inviscid disturbances.

In fact, neglecting $O(Re^{-1})$ terms not only removes the viscous and non-parallel terms, but also the Coriolis and streamline curvature terms, and the axial velocity component of the basic flow. This is the reason that inviscid stability results for the rotating disk can be applicable to a much wider class of cross-flow stability problems.

The resulting ordinary differential equations for the disturbance quantities can then be reduced to the Rayleigh equation

$$(Q - c)(w'' - \gamma^2 w) - Q''w = 0 \tag{2.4}$$

where primes denote differentiation with respect to z,

$$Q = U + \frac{\beta}{\rho\alpha}V, \quad \gamma^2 = \alpha^2 + \left(\frac{\beta}{\rho}\right)^2, \quad c = \frac{\omega}{\rho\alpha}, \tag{2.5a, b, c}$$

where U and V are the radial and azimuthal components of the basic flow respectively (note that $\lim_{z\to\infty} U = 0$ and $\lim_{z\to\infty} V = -1$). When α and β are real, Q can be interpreted as the basic flow resolved in the direction of the wavevector of the disturbance, and (2.4) then corresponds directly to (1.1). However, in the spatio-temporal analyses presented here, complex α are considered, and then Q has no immediate physical interpretation.

Roots of the dispersion relation are found by solving (2.4) numerically for some real value of β/ρ and finding complex values of α and ω/ρ such that the solution for w satisfies the homogeneous boundary conditions

$$w(\rho, 0) = 0, \quad \lim_{z\to\infty} w(\rho, z) = 0. \tag{2.6a, b}$$

In practice, we choose a suitably large finite numerical value of $z = z_\infty$ where Q has essentially reached its asymptotic value $Q = -\beta/(\rho\alpha)$. At $z = z_\infty$ the solution is taken to be proportional to

$$w = \exp(-\sqrt{\gamma^2}z) \tag{2.7}$$

and the boundary condition (2.6*b*) is replaced by two initial conditions

$$w(\rho, z_\infty) = 1, \quad w'(\rho, z_\infty) = -\sqrt{\gamma^2} \qquad (2.8a, b)$$

and either α or ω/ρ is iterated until (2.6*a*) is satisfied to within some prescribed tolerance. When solutions with exponentially divergent eigenfunctions are required, (2.8) is replaced by

$$w(\rho, z_\infty) = 1, \quad w'(\rho, z_\infty) = \sqrt{\gamma^2}. \qquad (2.9a, b)$$

The branch-cuts still lie along the imaginary axes of the complex α-plane, but now their branch points have moved away from the origin to $\alpha = \pm i\beta/\rho$, leaving an analytic strip of finite thickness along the real α-axis near the origin.

Due care is required with regard to any critical points, $z = z_c$, where $Q(z_c) = c$, since the solution generally has a logarithmic singularty at a critical point, unless $Q''(z_c) = 0$, see Drazin & Reid (1981). The integration path in the complex z-plane must pass the correct side of each critical point in order to remain on the correct branch of the complex logarithm and so obtain the correct phase jump across the critical point. The correct path lies along the real axis when the wavenumbers are real and the frequency has sufficiently large positive imaginary part, i.e. the original configuration of integration contours in the complex frequency and wavenumber planes used in constructing the solution to an initial-value problem. This is because then the critical points all lie away from the real z-axis (c is then complex, but Q is real for real z and real wavenumbers) and the solution to a well-posed linear problem will remain continuous and differentiable along the real z-axis if the initial condition is.

However, we are particularly interested in finding the correct paths of integration for the eigenvalues, and these can be found by lowering the frequency contour towards the eigenvalues while following the trajectories of the critical points in the complex z-plane. If a real wavenumber is chosen such that there is a frequency eigenvalue with positive imaginary part, then reducing the imaginary part of the frequency towards its value at the eigenvalue will not cause any critical points to cross the real z-axis, and the path of integration can remain on the real z-axis. If the wavenumber is then adjusted, one or more of the critical points may cross the real z-axis, in which case the integration path must be moved away from the real z-axis so as to remain on the same side of the critical points. A quick calculation shows that the critical points approach the real z-axis from above if $\alpha Q'(z_c) > 0$ when z_c and the wavenumbers are real, and from below if $\alpha Q'(z_c) < 0$, therefore corresponding to the rule given by Lin (1955) based on a consideration of the behaviour of the viscous problem as the Reynolds number tends to infinity.

The selection of the path around a critical point specifies the branch of the complex logarithmic function that is being used, and hence specifies whether the branch-cut from the critical point has $z \to i\infty$ or $z \to -i\infty$ along it. For example, figure 2(*a*) shows a possible position for this branch-cut when the integration path lies below the critical point. This branch-cut in the complex z-plane maps to a branch-cut in the complex frequency plane, see figure 2 of Huerre & Monkewitz (1985), and therefore, as mentioned in the Introduction, contributes a continuous spectrum to the physical solution.

The addition of viscosity regularizes the solution near the critical point, and the viscous solution decays along the real axis in both directions away from the critical point. However, the viscous solution does not decay in all directions away from the critical point in the complex z-plane. In the viscous calculation there are three Stokes lines radiating from the critical point where the viscous solutions can change from
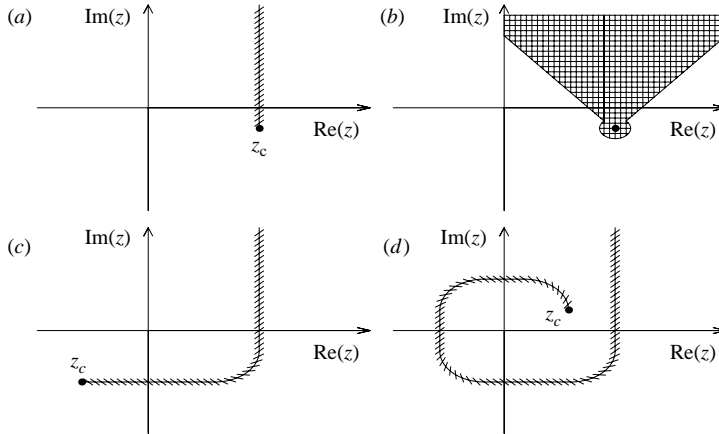
FIGURE 2. (*a*) Positions of a critical point z_c, and branch-cut (hatched line), in the complex z-plane giving rise to a quasi-mode, where the path must be taken below the real z-axis. (*b*) Shaded area indicates the region where the viscous solution dominates when a small amount of viscosity is introduced (but the viscous wall layer is not shown). (*c*, *d*) Schematic the arrangements of critical points and their branch-cuts of more exotic quasi-modes that have been found during the course of the present investigation.

decaying to growing exponentially with distance from the critical point. Matching with the surrounding inviscid solution can be achieved by arranging for the viscous solutions to decay in sectors that include the real z-axis, but there remains a third sector where the viscous solution grows exponentially, see Lin (1955). This situation is illustrated schematically in figure 2(*b*), where the bulge surrounding the critical point represents the thickness of the viscous critical layer, and the two Stokes lines that bound the exponentially growing viscous solution are included (the third Stokes line drops vertically downwards from the critical point).

Note that when the inviscid solution has been obtained by moving the integration path away from the real z-axis the solution is no longer defined along the whole real axis, and a discontinuity exists in the eigenfunction where the path leaves, and then returns to, the real z-axis. The position of this discontinuity is arbitrary. Such solutions are clearly not physical, and have been called 'quasi-modes', see Briggs, Daugherty & Levy (1970), but they are nonetheless of physical interest for at least two reasons. First, the quasi-mode corresponds to the solution of the viscous version of the problem at large Reynolds numbers, essentially because the dispersion relation in both cases can be obtained by taking the same path in the complex z-plane along which viscous terms are negligible (but if the Reynolds number is not large enough the point $z = 0$, where boundary conditions are applied, may lie inside the viscous critical layer, and then the viscous solution will differ significantly from the inviscid solution). In the plasma physics literature, these quasi-modes are also referred to as Landau poles, and their associated exponential decay referred to as Landau damping. Secondly, even in the inviscid problem, quasi-modes have been shown to represent the behaviour of the solution of initial value problems for a certain range of intermediate asymptotic times, see Shrira & Sazonov (2001). In previous studies quasi-modes have always been damped, but in the present calculation the dominant unstable saddle point can be a quasi-mode, i.e. representing an unstable Landau pole. Examples were also identified where more complicated arrangements of critical points and branch-cuts occur, see figure 2(*c*, *d*), that seem to break the correspondence between quasi-modes

and viscous modes because the viscous sector shown in figure 2(*b*) engulfs the origin no matter how large the Reynolds number is.†

Calculating quasi-modes requires obtaining the basic flow profiles for complex values of *z*, which can be realized by carrying out numerical integration of the basic flow equations along the same path in the complex *z*-plane that is required in solving the Rayleigh equation, as in Healey (1998). Or, if only relatively small continuations are needed in the complex *z*-plane, a model, e.g. Padé approximants or Chebyshev polynomials, could be fitted to the real basic profile and then evaluated for complex *z*. However, in the present case neither of these approaches is necessary, because we were able to obtain an analytic solution for the basic flow by taking a large-*z* asymptotic expansion for the basic flow that converges even for $z = 0$, see Healey (2006) for details.

Finally, we end this section by presenting the formal solution to the initial-value boundary-value problem for disturbances to the rotating-disk boundary layer in terms of inverse Fourier transforms, which will be solved in subsequent sections by both numerical and asymptotic methods. Note that the basic flow is assumed to be parallel, so that the WKB formulation (2.3) can be replaced by Fourier modes. The solution can therefore only be followed over distances over which the basic flow does not change significantly, though this distance can be made arbitrarily large by increasing *Re*.

A time-dependent forcing $\hat{f}(t)$ of given integer azimuthal wavenumber $n = \beta Re$ is switched on at time $t = 0$, at radius $r = r_0$, on the disk surface $z = 0$, giving the boundary condition

$$\hat{w}(r, \theta, 0, t) = \delta(r - r_0)\hat{f}(t)e^{in\theta}, \tag{2.10}$$

where $\hat{f} = 0$ for $t < 0$ and the flow is undisturbed before the forcing is switched on. Fourier transforms are taken of this boundary condition and the disturbance equations, leading to the Rayleigh equation for $w(z; \alpha, \beta/\rho, \omega/\rho)$ (but in what follows we shall only make explicit the dependence of *w* on *z*), the Fourier transform of $\hat{w}$. The physical solution is then obtained by evaluating the following double inverse Fourier transform:

$$\hat{w}(r, \theta, z, t) = \frac{e^{in\theta}}{4\pi^2} \int_A \int_F \frac{f(\omega)}{\Delta} w(z) \exp iRe(\alpha\rho - \omega t)\, d\omega\, d\alpha \tag{2.11}$$

where $\Delta(\alpha, \beta/\rho, \omega/\rho) = 0$ is the dispersion relation (the roots of which give the non-trivial solution to the homogeneous problem $f = 0$). The integration contours *F* and A run from $-\infty$ to $+\infty$, with A lying along the real axis of the complex α-plane (which is free from singularities because at finite *t* the disturbance produced by $\hat{f}$ only extends over a finite range of *r*, ensuring the convergence of the α-integral), and *F* lying above all singularities in the complex ω-plane, corresponding to the Bromwich contour in Laplace transforms (to respect the principle of causality). A disturbance localized in the azimuthal direction as well can then be constructed by summing over *n*, but we shall study particular real values of *n*, or equivalently, real β/ρ.

It is possible to determine the propagation properties of a disturbance without evaluating the double integral (2.11). Briggs (1964) showed that this can be accomplished through a consideration of the behaviour of the roots of the dispersion relation $\Delta = 0$ and their positions relative to the contours of integration *F* and A. As mentioned in §1, we seek to lower *F* to just below the real axis of the complex

† These calcuations are available in an online supplement to this paper.

ω-plane to discover whether the temporal instability can be transformed into a spatial instability, and if it can be, to identify the direction of propagation. A point on F may generate a number of points in the α-plane that are roots of $\Delta = 0$. The loci of these roots in the α-plane generated by moving ω along F are called spatial branches. The spatial branches are plotted for a range of heights of F in the complex frequency plane. When F is high enough the spatial branches are confined either to the upper half-plane (downstream propagating modes) or the lower half-plane (upstream propagating modes). If a spatial branch crosses the real α-axis as F is lowered, then the A contour is deformed away from the real axis, as in figure 1(b), to remain on the same side of the branch. However, F cannot be lowered to below a critical value of $\mathrm{Im}(\omega)$ where downstream and upstream spatial branches coalesce since then A becomes pinched between the branches. Such a point is called a pinch point, and it signifies absolute instability if $\mathrm{Im}(\omega) > 0$ at the pinch point.

However, it will be more convenient here to interpret the pinch point as a saddle point of the dispersion relation. These saddle points arise in the large-time asymptotic estimation of (2.11), which allows an actual calculation of the propagating wavepacket to be carried out, rather than simply classifying a flow as being convectively or absolutely unstable. Therefore, we shall now focus attention on the case of impulsive forcing $\hat{f}(t) = \delta(t)$, where $\delta(t)$ is the Dirac delta function, and hence $f = 1$. The F contour is closed in the lower half of the complex ω-plane and evaluated as the sum of the residues of the poles produced by simple zeros of $\Delta = 0$,

$$\hat{w}(r, \theta, z, t) = \sum_m -\frac{\mathrm{i}e^{\mathrm{i}n\theta}}{2\pi} \int_A \frac{w(z)}{\Delta_\omega} \exp \mathrm{i}Re(\alpha\rho - \omega_m t) \, \mathrm{d}\alpha \qquad (2.12)$$

where $\omega_m = \omega_m(\alpha)$ is the mth root of $\Delta = 0$ (ω_m also depends on β/ρ, but we are considering the evolution of a particular azimuthal wavenumber with fixed β/ρ). Equation (2.12) is in the standard form for application of the method of steepest descents, where, as $t \to \infty$ and $\rho/t = O(1)$, the integral is dominated by the contributions from certain saddle points of the function ϕ_m,

$$\phi_m = \mathrm{i}Re \left(\alpha\frac{\rho}{t} - \omega_m \right) \qquad (2.13)$$

satisfying $\mathrm{d}\phi_m/\mathrm{d}\alpha = 0$, i.e.

$$\frac{\mathrm{d}\omega_m}{\mathrm{d}\alpha} = \frac{\rho}{t}, \qquad (2.14)$$

see Wong (1989).

However, not all saddles contribute to the integral. For a saddle to make the dominant contribution, it must be possible to deform A so that it lies entirely within the valleys of the saddle. A saddle can sometimes contribute to the solution even when A is not contained by its valleys; such a saddle is called subdominant. The deformations of A need to be considered for each Riemann surface, i.e. for each index m. Examples of saddles that contribute to the integral (relevant saddles) and those that do not (irrelevant saddles) are given below. Saddles are found by plotting contours of constant $\mathrm{Re}(\phi_m)$ in the complex α-plane for a frame of reference moving at a given constant velocity ρ/t. For the rest frame $\rho/t = 0$, constant $\mathrm{Re}(\phi_m)$ corresponds to constant $\mathrm{Im}(\omega_m)$, and therefore the contours of constant height surrounding the saddle point correspond to the spatial branches obtained for various F with constant imaginary parts of the frequency. The spatial branches at the pinch point therefore correspond to the boundaries of the valleys of the highest saddle, and since the integration contour A lies within these valleys the pinch point is the dominant saddle in

the rest frame. However, as ρ/t is moved away from zero, the saddles will move in the complex α-plane, and their relative heights will change, so that for any given ρ/t the dominant saddle need not be the continuation of the pinch point of the rest frame.

Note, however, that in some papers the pinch point is referred to as a branch point instead of as a saddle point. In this paper, the pinch point will always refer to the dominant saddle point of the complex wavenumber plane. We shall use the term branch point to refer exclusively to a point in the complex wavenumber plane where two Riemann surfaces meet, e.g. at which $d\phi_m/d\alpha \to \infty$, or when $\gamma^2 = 0$. Branch-cuts can be drawn from branch points to separate the Riemann surfaces (but not from saddle points).

3. Behaviour of the pinch point as wavelengths increase

In this section the spatial branches, and pinch points, of the inviscid dispersion relation obtained by numerical integration of (2.4), with boundary conditions (2.6a) and (2.8) or (2.9), are investigated as β/ρ is reduced towards zero for the rest frame $\rho/t = 0$. Figure 3(a) shows spatial branches when $\beta/\rho = 0.036$ for a range of constant values of $\mathrm{Im}(\omega)$, including values corresponding to two saddle points. However, this figure is difficult to interpret because spatial branches, i.e. contours of different heights of $\mathrm{Re}(\phi_m)$, intersect one another at points in the complex α-plane. These intersections arise because there are two temporal branches, i.e. two values of ω_m satisfying $\Delta = 0$, for each value of α, corresponding to different values of the frequency subscript m. The spatial branches are contours of a multi-valued surface, and their 'intersections' are artifacts generated by projection down onto the complex α-plane. The two (Riemann) surfaces meet at a branch point where $d\alpha/d\omega_m = 0$. Following one root of the dispersion relation along a closed path around this branch point in the complex α-plane leads continuously to the other root of the dispersion relation, giving rise to a certain ambiguity in the labelling of the roots denoted by the subscript m.

It is convenient to remove this ambiguity by introducing a branch-cut radiating away from the branch point, which defines the extent of a particular root, and is essentially an instruction to switch from one surface to another (i.e. from one temporal branch to another). The position of the branch-cut is arbitrary (it only has to terminate at the branch point) and does not affect the value of the integral (2.12). Figures 3(b) and 3(c) show the two single-valued surfaces obtained by choosing the branch-cut to drop vertically downwards from the branch point in the complex α-plane. The summation over m in (2.12) implies that the physical solution will be the sum of the integrals along paths across each surface shown in figures 3(b) and 3(c). Both surfaces have the property that the real α-axis for large $|\mathrm{Re}(\alpha)|$ lies within the valleys of the saddle points, and so both saddle points contribute to the physical solution, with the one shown in figure 3(b) making the dominant contribution since it has the larger $\mathrm{Im}(\omega_m)$, thus corresponding to the pinch point.

Note that, for example, if the branch-cut is chosen instead to lie vertically above the branch point, then both saddles would be accessible to the same integration contour. In this case the contour would pass over the saddle shown in figure 3(b), down the right-hand valley of this (dominant) saddle, below the branch point, and up the right-hand side of the branch-cut (now vertically above the branch point) descending, as it does so, from a hill into the left-hand valley of the saddle in figure 3(c). From here, it passes over this saddle into its right-hand valley and ultimately to the positive real α-axis. This illustrates how a subdominant saddle can make an exponentially
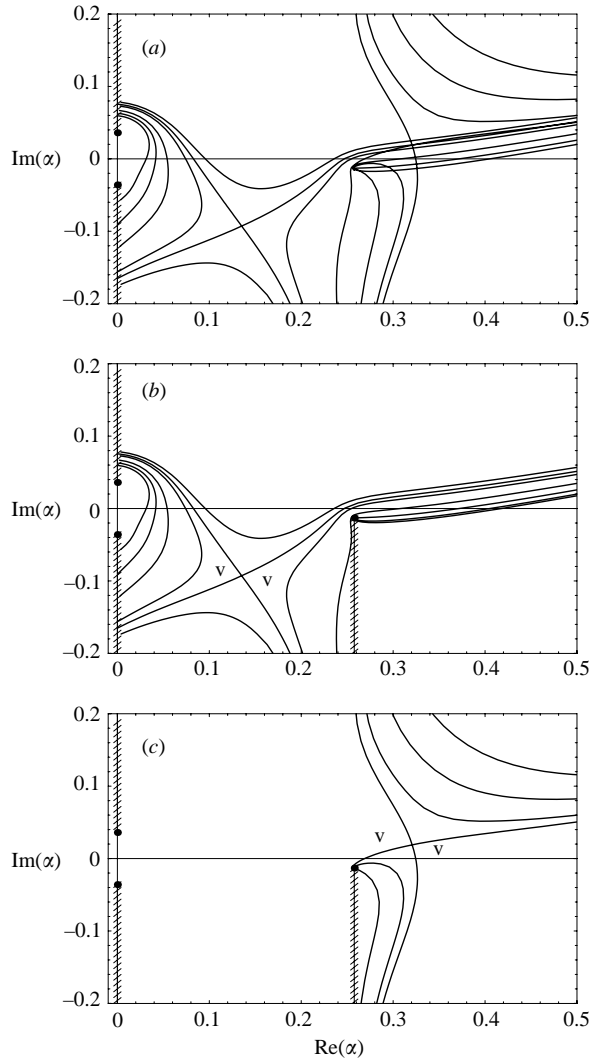
FIGURE 3. Numerical solutions for the spatial branches for various constant $\text{Im}(\omega_m)$ and $\beta/\rho = 0.036$. Hatched lines on the imaginary axes represent branch-cuts with branch points at $\alpha = \pm i\beta/\rho$. There are saddle points at $\alpha = 0.1352 - 0.0928i$, $\omega_m = 0.000134 + 0.005824i$ and at $\alpha = 0.3207 + 0.0189i$, $\omega_m = 0.002950 + 0.001717i$, where $d\omega_m/d\alpha = 0$. There is a branch point at $\alpha = 0.2577 - 0.0131i$, $\omega_m = 0.005468 + 0.002566i$, where $d\alpha/d\omega_m = 0$, from which a branch-cut has been introduced in (b) and (c). The valleys of each saddle are indicated by a v.

small contribution to the solution, but that to capture this saddle's contribution it may be necessary to take a path that includes part of a hill of the saddle. However, in what follows, we shall generally, in the first instance, place branch-cuts vertically and so as not to cross the real α-axis. Nonetheless, figure 3 shows the importance of investigating the Riemann surfaces 'behind' any branch-cut, because if only the surface shown in figure 3(c) had been investigated, then although a saddle would have been found that looks like a pinch point, it is only by considering the continuation of this surface beyond the branch-cut, i.e. the surface shown in figure 3(b), that the true dominant contributing saddle can be found.
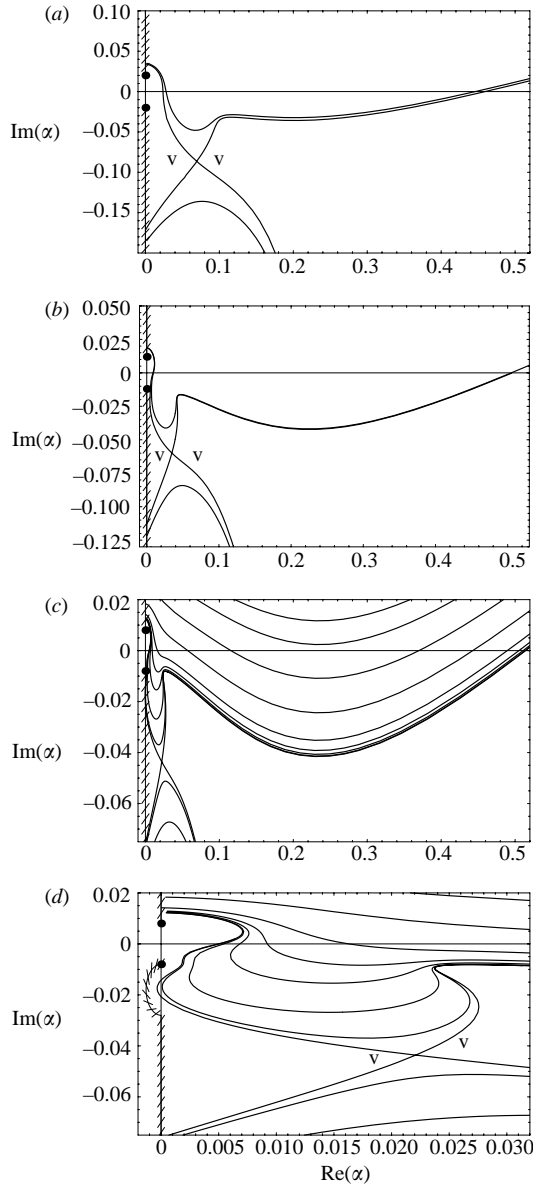
FIGURE 4. Numerical solutions for the spatial branches for various constant $\text{Im}(\omega_m)$ for (a) $\beta/\rho = 0.02$; (b) $\beta/\rho = 0.012$; (c) $\beta/\rho = 0.008$; (d) is a detail of (c). Hatched lines are branch-cuts with branch points at $\alpha = \pm i\beta/\rho$. Valleys of the saddles (pinch points) are indicated by a v.

Both saddles in figure 3 correspond to saddles found analytically in the small-β/ρ long-wave theory presented in Healey (2006). That theory showed that the saddle in figure 3(b) dominates the saddle in figure 3(c) as $\beta/\rho \to 0$. However, it also predicts that the saddle of figure 3(b) approaches the imaginary axis of the complex α-plane. We now reduce β/ρ to investigate the consequences of this latter prediction.

Figure 4(a–c) shows the progression of the pinch point, and spatial branches, towards the negative imaginary axis as β/ρ is reduced. Note that the numerical

solution for the spatial branches near the positive imaginary axes of the diagrams becomes increasingly challenging for small β/ρ. As discussed in Healey (2005), this is because in this limit the phase velocity approaches the velocity at the point where $Q'(z) = 0$, and this point moves further from the real z-axis. Therefore, the two critical points become asymptotically close to one another, and lie an $O(1)$ distance from the real z-axis. The integration path must lie above one of these critical points, and below the other, requiring a path to be taken between the two. As the critical points approach each other the integration path becomes trapped between them, causing the numerical difficulties. In practice, therefore, we expect viscosity to be particularly important in this part of the complex α-plane.

It can be seen in figure 4(*d*) that when $\beta/\rho = 0.008$ the dominant saddle can only be reached by moving a part of the branch-cut to the left of the imaginary α-axis. For $\beta/\rho > 0.008424$ the saddle can be reached without moving the branch-cut from the imaginary α-axis, giving the standard pinch-point behaviour reported by Lingwood (1995). For $\beta/\rho < 0.008424$ the saddle can only be reached by moving the branch-cut as indicated in figure 4(*d*), and this corresponds to the behaviour predicted by the long-wave theory of Healey (2006), see figure 4 of that paper for the corresponding diagram. Therefore, the inviscid stability problem for the rotating-disk boundary layer gives rise to the scenario shown in figure 1(*c*).

However, as discussed in the Introduction, moving the branch-cut as indicated in figure 4(*d*) corresponds to choosing the solution to (1.2) that diverges exponentially in the wall-normal direction, i.e. taking $C_1 = 0$, $C_2 \neq 0$ in (1.3). Such a solution does not satisfy homogeneous boundary conditions, which might lead one to argue that therefore the branch-cut cannot be moved in this way. Nonetheless, the physical solution does not depend on the position of the branch-cuts. After all, the physical solution can be calculated by performing the integration along the real α-axis instead; the deformation of the α-integration contour to pass through the steepest descent path of the saddle point is only required in order to make an asymptotic large-time estimate of the solution to the impulsive forcing.

And yet, there is a physical consequence of spatial branches with $\text{Im}(\omega_m) > 0$ crossing the imaginary α-axis as in figure 4(*d*). An idea of the possible physical consequences can be obtained by considering for a moment the disturbance generated by a periodic forcing with frequency within the interval that generates that part of the spatial branch that crosses the imaginary α-axis. Although a normal mode with such a frequency would have an exponentially diverging eigenfunction, one should really only consider the evolution of the disturbance from a prescribed initial-value problem. The flow is undisturbed for $t < 0$, and after any large enough finite time a normal-mode-like structure will be set up, growing in the wall-normal direction as it propagates away from the disturbance source out into the undisturbed flow above the source. The disturbance will thus always satisfy homogeneous boundary conditions, but can, in principle, show exponential growth in the wall-normal direction over some finite, but increasing, distance from the wall.

However, a question remains over where the energy comes from in order to sustain an exponential growth in the wall-normal direction, since far from the wall there is no basic flow shear, and hence no Reynolds stress. Also, since the present flow is absolutely unstable, does it even make sense to consider the response to periodic forcing described in the preceeding paragraph? These issues will be addressed in the following sections where detailed asymptotic and numerical studies of solutions of initial-value problems for the inviscid rotating-disk boundary layer will be carried out.

4. Convective instability in the wall-normal direction

The advection of disturbance energy by the disturbance velocity is a nonlinear process, e.g. see equation (5.25) of Drazin (2002). Nonetheless, the question of how a disturbance can grow in amplitude in the absence of a local source of energy can be addressed by considering the propagation characteristics of the disturbance within the linear theory.

4.1. *Wall-normal propagation*

Our interest lies principally in the evolution of an impulsive disturbance as it propagates outside the boundary layer, and the possibility that this can lead to a disturbance structure with exponential growth in the wall-normal direction. Therefore, we shall combine the exponential form of the solution outside the boundary layer (2.7) with the impulse response (2.12) to give

$$\hat{w}(r, \theta, z, t) = \sum_m -\frac{\mathrm{i}e^{\mathrm{i}n\theta}}{2\pi} \int_A \frac{1}{\Delta_\omega} \exp Re\left[\mathrm{i}(\alpha\rho - \omega_m t) - \sqrt{\gamma^2}\zeta\right] \mathrm{d}\alpha, \qquad (4.1)$$

where $z = Re\,\zeta$, and ζ is the axial coordinate scaled in the same way as the radial coordinate (2.2). At large times this solution is dominated by the contribution made to the integral by appropriate saddle points of the exponent

$$\phi_m = Re\left[\mathrm{i}\left(\alpha\frac{\rho}{t} - \omega_m\right) - \sqrt{\gamma^2}\frac{\zeta}{t}\right] \qquad (4.2)$$

satisfying $\mathrm{d}\phi_m/\mathrm{d}\alpha = 0$, i.e.

$$\frac{\mathrm{d}\omega_m}{\mathrm{d}\alpha} = \frac{\rho}{t} + \frac{\mathrm{i}\alpha}{\sqrt{\gamma^2}}\frac{\zeta}{t}. \qquad (4.3)$$

The addition of the second term in (4.3) allows the disturbance to be calculated in frames of reference moving in the wall-normal direction. When there is a normal mode that decays exponentially in the wall-normal direction and $\zeta/t > 0$, the corresponding term makes a stabilizing contribution to the growth rate $Re(\phi_m)$ of (4.2). However, if the dominant saddle point found by solving (4.3) moves across the imaginary axis of the complex α-plane then, in effect, the square-root term in (4.2) changes sign, and then the ζ/t term makes a destabilizing contribution to the disturbance, reflecting the exponential growth in the eigenfunction.

The saddle points of figures 3 and 4 correspond to the rest frame $\rho/t = \zeta/t = 0$. When ζ/t is increased from zero, the dominant saddle point is found to move towards the imaginary α-axis, see for example figure 5(*a*), where this saddle (marked A) has almost reached the imaginary axis. Figure 5(*a*) also shows the existence of another saddle point (marked B) constructed from an exponentially divergent eigenfunction, though for these parameter values it is not the dominant saddle. However, the arrangement of the valleys of each saddle is such that the integration countour in the complex α-plane can be deformed to pass through both of them, so they both contribute to the physical solution, even the one with divergent eigenfunction. Note that the integration path approaching from the left of these figures lies on the Riemann surface of decaying eigenfunctions, while the dashed lines in the left half-plane are spatial branches for growing eigenfunctions. The integration path passes over this second Riemann surface only after it has travelled around the branch point at $\alpha = -\mathrm{i}\beta/\rho$.

Figure 5(*b*) shows the effect of increasing ζ/t further. Both saddle points are now made up of divergent eigenfunctions, and saddle B has become the dominant saddle,
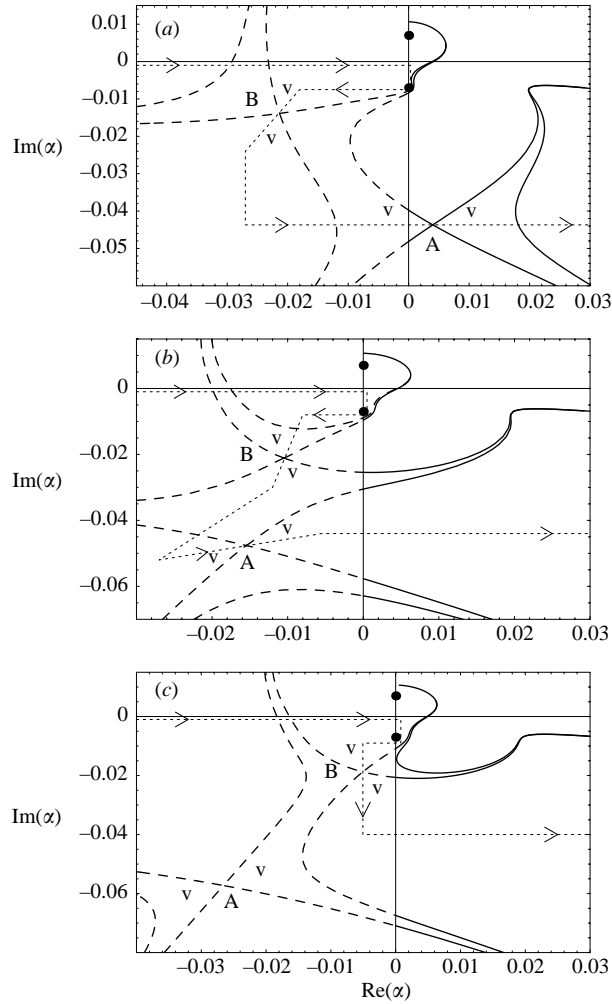
FIGURE 5. Contours of constant $\mathrm{Re}(\phi_m)$ given by (4.2) for $\beta/\rho = 0.007$, $\rho/t = 0$ and (a) $\zeta/t = 0.001$; (b) $\zeta/t = 0.0018$; (c) $\zeta/t = 0.0024$. Dashed lines indicate eigenvalues with exponentially divergent eigenfunctions, solid lines have exponentially decaying eigenfunctions that satisfy homogeneous boundary conditions. Solid circles at $\alpha = \pm \mathrm{i}\beta/\rho$ give the branch points where these roots coalesce, but the branch-cuts terminating at these branch points are not shown. Valleys of saddles are indicated by a v. Dotted lines with arrows are examples of paths of integration. The saddle marked A corresponds to the pinch point in the rest frame, i.e. the saddles shown in figure 4.

though saddle A still makes a contribution to the solution because the integration contour can be brought down the valley from B into the valley to the left of A, then over the saddle A along A's steepest descent path, and finally back to the positive real α-axis within a valley of both A and B. The effect of a further increase in ζ/t is shown in figure 5(c). Although saddle A is now higher than saddle B, saddle B remains the dominant saddle, and A makes no contribution to the solution. This is because the valleys of A do not contain the end-points of the integration contour, while the valleys of B do, and the integration contour following the steepest descent path through B cannot reach A without leaving the valleys of B.
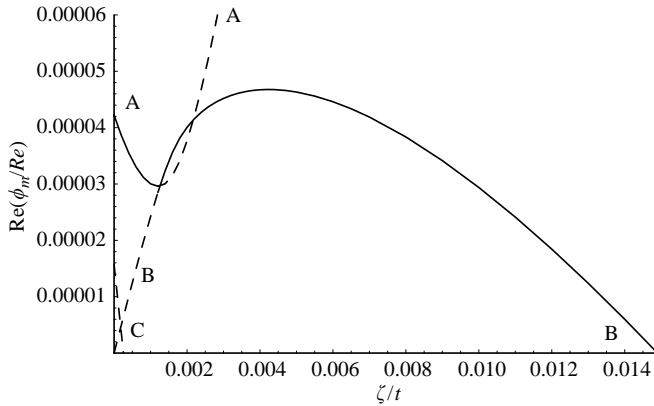
FIGURE 6. Growth rates predicted by saddles of (4.2) when $\beta/\rho = 0.007$ and $\rho/t = 0$. Solid lines indicate the dominant saddle, dashed lines indicate saddles that are either subdominant, or irrelevant. The labels A and B correspond to the saddles shown in figure 5, C corresponds to the saddle shown in figure 3(c).

The contribution of saddle A is switched off at $\zeta/t = 0.00216$, where the two saddles have the same height, but there is no associated discontinuity in the solution, because as the heights of the saddles approach one another, the integration contour from B to the left-hand valley of A runs between a pair separatrices from each saddle, and then the contribution from the path back over the saddle A almost cancels that of the path coming down the hill of A. This cancellation significantly reduces the contribution of the saddle A when it is just below B, and smoothly reduces its contribution to zero as A overtakes B in height. The integral representation of the Airy function, Ai, provides a model problem with two saddles whose heights can change in the manner shown in figure 5, see Hinch (1991). Situations where both saddles contribute, where dominance is exchanged, and where one saddle ceases to contribute have been investigated and the corresponding saddle-point theories compared with direct evaluation of the integral.†

The sequence of diagrams in figure 5(a–c) shows the necessity of mapping out the separatrices of the saddles (i.e. the level curves passing through the saddles) to determine which is dominant. The diagrams also show the importance of parameter values where saddles are at the same height, even if they are widely separated in the complex α-plane, since at these values either the dominance can change, or a saddle can become irrelevant to the solution.

These principles have been used to obtain figure 6, which shows the growth rates (heights) of these two saddles over a range of ζ/t and indicates the dominant saddle at any given ζ/t. The change in dominance from saddle A to saddle B seen between figures 5(a) and 5(b) corresponds to the intersection near $\zeta/t = 0.00127$. The subsequent onset of the irrelevance of A seen between figures 5(b) and 5(c) corresponds to the intersection near $\zeta/t = 0.00216$. The result is that while the growth rate of the absolute instability in the rest frame $\zeta/t = 0$ is determined by saddle A, the leading edge of the wavepacket, which propagates in the wall-normal direction at velocity $\zeta/t = 0.0149$ is controlled by saddle B. At $\zeta/t = 0$, A is composed of eigenfunctions that decay in the wall-normal direction, and so increasing ζ/t reduces the growth rate of the dominant saddle as discussed following (4.3). Similarly, the

† These calculations are available in an online supplement to this paper.

eigenfunctions for C decay even more rapidly, since C lies further from the imaginary α-axis, and this causes a stronger stabilization as $\zeta/t=0$ increases. However, at $\zeta/t=0$, B is composed of eigenfunctions that diverge in the wall-normal direction, and so increasing ζ/t increases the growth rate of this saddle. The initial decay of A, and growth of B, are clear at the left of figure 6, and lead to the first intersection of these two curves at $\zeta/t=0.00127$, transfering dominance to the saddle whose growth rate increases with increasing ζ/t. Furthermore, this figure shows that the growth rate of B continues to increase with increasing ζ/t such that the maximum growth rate occurs for a finite positive value of $\zeta/t=0.0042$.

This last observation means that at any given moment (large enough for the saddle-point theory to be accurate) the largest amplitude of the disturbance in the wall-normal direction lies outside the boundary layer, and this position of maximum amplitude is moving further outside the boundary layer, with this amplitude growing all the time. We now show that the existence of a maximum growth outside the boundary layer is intimately related to the existence of a spatial branch crossing the imaginary α-axis.

4.2. *Spatial branch touching the imaginary axis*

First note that there is a well-known result concerning the more usual streamwise propagation problem, in which the maximum growth rate occurs when the saddle point crosses the real α-axis (any minimum in growth rate also occurs when the saddle has real wavenumber, but in what follows we shall sometimes use 'maximum' instead of 'stationary', because this is the focus of our interest). When $\zeta/t=0$, a saddle point with real α has stationary growth rate, $\text{Re}(\phi_m)$ in (4.2), with respect to ρ/t because the coefficient of ρ/t then has zero real part, so that small changes in ρ/t do not change the growth rate. Furthermore, the point on the real α-axis at which the saddle crosses the real α-axis is the real wavenumber with maximum temporal growth. Considering saddles with real wavenumbers in (4.3) gives

$$\frac{d\omega}{d\alpha} = \frac{\partial \omega_r}{\partial \alpha_r} + i\frac{\partial \omega_i}{\partial \alpha_r} = \frac{\rho}{t} \qquad (4.4)$$

where subscripts r and i denote real and imaginary parts respectively (and the subscript m has been, and will be, dropped when doing so causes no ambiguity). Equating real and imaginary parts of (4.4) gives

$$\frac{\partial \omega_r}{\partial \alpha_r} = \frac{\rho}{t}, \qquad \frac{\partial \omega_i}{\partial \alpha_r} = 0, \qquad (4.5a,b)$$

where (4.5b) is the condition for maximum growth rate in a temporal stability analysis.

This argument is readily adapted to the present case of wall-normal propagation with $\zeta/t \neq 0$ and $\rho/t=0$. The growth rate is stationary with respect to ζ/t when the coefficient of ζ/t in (4.2) has zero real part, i.e. when the saddle lies on the imaginary axis of the wavenumber plane. Considering saddles with purely imaginary wavenumbers in (4.3) gives

$$\frac{d\omega}{d\alpha} = \frac{\partial \omega_i}{\partial \alpha_i} - i\frac{\partial \omega_r}{\partial \alpha_i} = \frac{i\alpha}{\sqrt{\gamma^2}}\frac{\zeta}{t} \qquad (4.6)$$
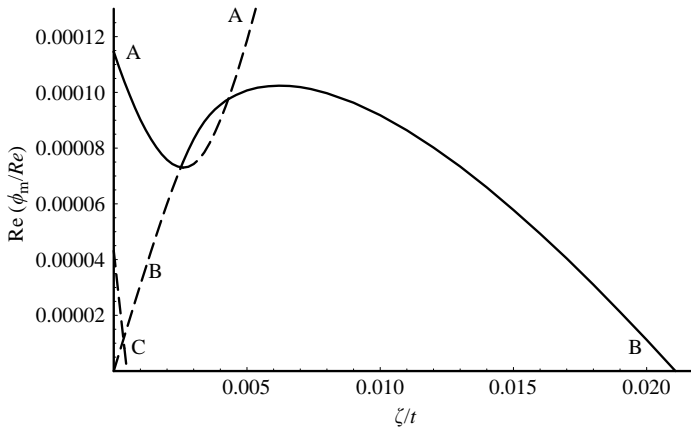
FIGURE 7. Growth rates predicted by saddles of (4.2) when $\beta/\rho = 0.01$. Solid lines indicate the dominant saddle, dashed lines indicate saddles that are either subdominant, or irrelevant. Saddles A, B and C correspond to those in figure 6.

and equating real and imaginary parts, for purely imaginary $\alpha = i\alpha_i$ with $|\alpha_i| > \beta/\rho$ (so that the saddle lies where the original branch-cuts were placed), gives

$$\frac{\partial \omega_i}{\partial \alpha_i} = 0, \quad \frac{\partial \omega_r}{\partial \alpha_i} = -\alpha_i \left[\alpha_i^2 - \left(\frac{\beta}{\rho} \right)^2 \right]^{-1/2} \frac{\zeta}{t} \qquad (4.7a, b)$$

where (4.7a) is the condition for maximum temporal growth rate for purely imaginary wavenumbers. With $\rho/t = 0$ and the coefficient of ζ/t purely imaginary, (4.2) shows that the growth rate is given by ω_i, and so by (4.7a), the maximum growth rate of the wavepacket in the wall-normal direction occurs in the frame of reference where the saddle point crosses the imaginary axis of the complex α-plane.

Therefore, the spatial branch that first touches the imaginary α-axis in figure 4(d) as ω_i is reduced, has ω_i corresponding to the maximum growth rate of the wall-normal propagating part of the wavepacket. If this branch has larger ω_i than the branches at the dominant saddle (pinch point), then the largest amplitude in the wall-normal direction will be outside, and propagating away from, the boundary layer. If this branch has smaller ω_i than the branches at the dominant saddle (pinch point), as in figure 4(b), then the largest amplitude in the wall-normal direction will be inside the boundary layer, which is the conventional situation. As mentioned earlier, for this inviscid rotating-disk boundary layer problem the changeover between the case where the spatial branch touching the imaginary axis has larger ω_i than at the dominant saddle, and the case where ω_i is larger at the dominant saddle, occurs at $\beta/\rho = 0.008424$. Figure 7 confirms that for $\beta/\rho = 0.01 > 0.008424$ the maximum growth does indeed occur inside the boundary layer (i.e. as $\zeta/t \to 0$), though the decay outside the boundary layer is not monotonic. It has also been verified that all the maxima and minima of the curves in figures 6 and 7 do occur when the corresponding saddle lies on the imaginary α-axis.

4.3. *Propagation of energy outside the boundary layer*

The question to be addressed now is how growth outside the boundary layer is possible when there is no source of energy for the disturbance outside the boundary since then there is no basic shear, and therefore zero Reynolds stress. The answer lies
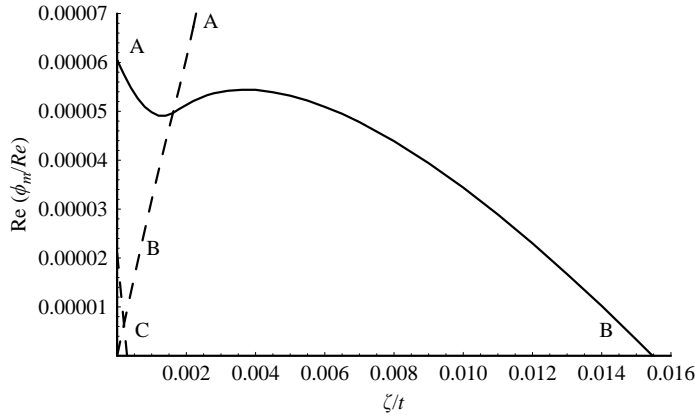
FIGURE 8. Growth rates predicted by saddles of (4.2) when $\beta/\rho = 0.007$ and $\rho/t = 0.0005$. Solid lines indicate the dominant saddle, dashed lines indicate saddles that are either subdominant, or irrelevant. Saddles A, B and C correspond to the saddles shown in figure 5 at the left and right ends of the curves, but there is a change in identity of the saddles A and B as ζ/t increases through 0.0012.

in considering the full propagation of an impulsive disturbance in both streamwise and wall-normal directions simultaneously.

We shall concentrate on $\beta/\rho = 0.007$, which is a case where the largest amplitude in the wall-normal direction is growing and propagating away from the boundary layer when $\rho/t = 0$. In essence, this investigation involves extending the results of figure 6 to a range of non-zero ρ/t. In particular, neutral curves where saddles have zero growth rates are followed in $(\rho/t, \zeta/t)$ space, so that the unstable region can be mapped out, and also the loci where saddles have the same growth rates, which can indicate where changes in the dominance of the saddles take place.

However, before presenting the loci of these neutral curves and the curves where saddles have coincident growth rates, compare first the results shown in figure 8, where $\rho/t = 0.0005$, with those in figure 6, where $\rho/t = 0$. An exchange in identities of the saddles labelled A and B has occurred, such that, for example, as A is followed from left to right in figure 8, it undergoes a metamorphosis, and emerges at the right of the diagram as saddle B. This behaviour is characteristic of an interaction between the saddles A and B and indicates that at a value of ρ/t in the range $0 < \rho/t < 0.0005$ there is a coalescence of saddle points. At such a point three spatial branches coincide, and the following conditions are satisfied:

$$\frac{\mathrm{d}\phi_m}{\mathrm{d}\alpha} = \frac{\mathrm{d}^2\phi_m}{\mathrm{d}\alpha^2} = 0. \qquad (4.8)$$

An example of this type of degenerate branch point was found in a viscous calculation for the rotating-disk boundary layer by Healey (2004) for the stationary frame $\rho/t = \zeta/t = 0$, and in that problem too it was associated with changes in the dominance of two saddle points. As the saddle points approach the coalescence point, their approximations to the solution (i.e. to the integral (2.12)) both become singular because $\mathrm{d}^2\phi_m/\mathrm{d}\alpha^2 \to 0$, while at the coalescence point itself, the solution depends on $\mathrm{d}^3\phi_m/\mathrm{d}\alpha^3$, and involves an algebraic term $t^{-1/3}$. However, Chester, Friedman & Ursell (1957) have shown how to construct a uniform asymptotic expansion in the neighbourhood of the coalescence point.
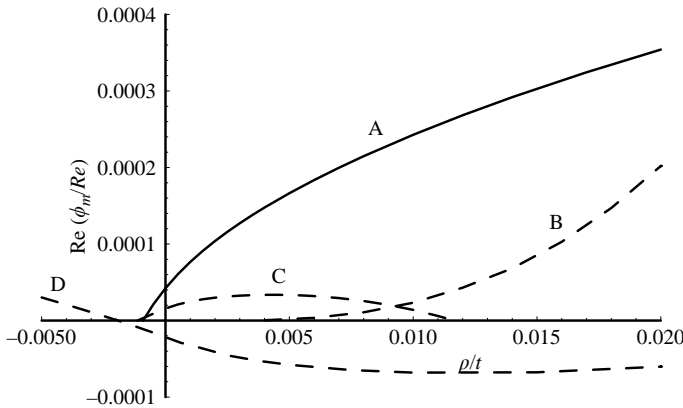
FIGURE 9. Growth rates predicted by saddles of (4.2) when $\beta/\rho = 0.007$ and $\zeta/t = 0$. Solid lines indicate the dominant saddle, dashed lines indicate saddles that are either subdominant, or irrelevant. Saddles A, B and C correspond to those at the left of figures 6 and 8.

Figures 6 and 8 also imply that in the $(\rho/t, \zeta/t)$-plane there will be three lines originating from this saddle coalescence point where saddles are at the same height, corresponding to the three intersections between the curves in these two figures. Only one of these three lines corresponds to a change in dominance of the saddles. We will encounter a number of saddle coalescence points in the $(\rho/t, \zeta/t)$-plane, and all will have three lines emanating from them where pairs of saddles have equal height, but only one, if any, of these lines will correspond to changes in the dominance of the saddles. Locating saddle coalescence points is therefore key to understanding the distribution of dominant saddles.

A further helpful step towards constructing the $(\rho/t, \zeta/t)$-plane is to generate the equivalent diagram to figure 6, but for $\zeta/t = 0$ and $\rho/t \neq 0$ instead. The growth rates of the saddles for a limited range of relatively small velocities ρ/t is shown in figure 9. Over the range of this figure, saddle A is dominant, except for $-0.00113 < \rho/t < -0.00082$, where C is the dominant unstable saddle. Note that C becomes a quasi-mode (as defined in §2) for $\rho/t > 0.005$ even though it is unstable (an example will be given later where the dominant unstable saddle is a quasi-mode).

More strangely, B, which has $\text{Re}(\alpha) < 0$ and a divergent eigenfunction, violates Howard's semi-circle theorem, Howard (1961). For $\rho/t < 0$ and $\zeta/t = 0$, the eigenvalues are real with $\alpha < 0$ and $\omega > 0$ giving a negative phase velocity, but since $\beta/(\rho\alpha) < 0$, $U \geqslant 0$ and $V \leqslant 0$ it follows from (2.5a) that $Q \geqslant 0$, i.e. the phase velocity does not lie between the minimum and maximum values of Q. In fact, Howard's semi-circle theorem, and the other theorems describing the stability of inviscid disturbances, like Rayleigh's inflection point theorem, are all derived by applying homogeneous boundary conditions, see Drazin & Reid (1981). Therefore, these derivations do not apply to modes with divergent eigenfunctions. Nonetheless, our results are consistent with Rayleigh's inflection point theorem. Healey (2006) shows that there are no inflection points for Q if $\phi < -37.57°$, where $\tan\phi = \beta/(\rho\alpha)$. This range corresponds to $-0.0091 < \alpha < 0$ for $\beta/\rho = 0.007$, and in this range the eigenvalues for B are all real.

The appearance of non-isolated real eigenvalues in a problem with a smooth continuous velocity profile is itself unusual because the critical points generally contribute imaginary terms to the dispersion relation. However, a real dispersion relation is possible if Howard's semi-circle theorem is violated, because then the
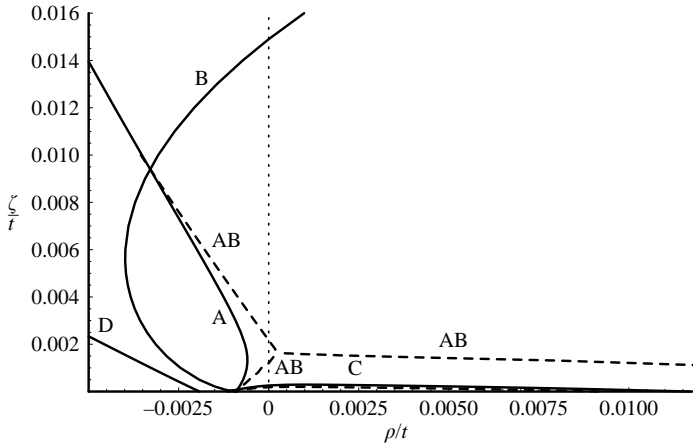
FIGURE 10. Solid lines are the neutral curves for the saddles A, B, C and D of figure 9 continued into the $(\rho/t, \zeta/t)$-plane for $\beta/\rho = 0.007$. The three dashed lines AB are loci where saddles A and B have the same growth rates; they meet at a three-way intersection point where saddles A and B coalesce at $\rho/t = 0.00025$, $\zeta/t = 0.00161$. The unlabelled dashed line immediately below the neutral curve for C represents the loci where saddles B and C have the same growth rates. A vertical dotted line is included at $\rho/t = 0$, separating upstream from downstream propagating parts of the disturbance.

critical points can lie at negative z, i.e. inside the plate. Critical points at negative z make no contribution to the dispersion relation if, as for B, the integration path passes along the real z-axis.

In fact, the four saddles shown in figure 9 are four of the saddles in the rest frame $\rho/t = \zeta/t = 0$ predicted by the long-wave asymptotic theory presented in Healey (2006). The wavenumbers of the saddles at leading order as $\beta/\rho \to 0$ are found by taking fourth roots of a real positive quantity, see (3.22) of Healey (2006), giving four solutions of the form $\alpha = \pm A_0$, $\pm i A_0$, where A_0 is real and positive. The saddle A, which is dominant in the rest frame, and which approaches the negative imaginary axis of the complex α-plane as $\beta/\rho \to 0$, corresponds to the root $-i A_0$. Saddle D, which is damped in the rest frame, corresponds to the root $i A_0$, and is the complex conjugate of A at leading order in β/ρ. However, D is a quasi-mode, and the small contribution from the critical points means it is not precisely the complex conjugate of A at finite β/ρ. The divergent mode B corresponds to the root $-A_0$, and the mode C corresponds to the root A_0.

We now consider the continuation of the results of figure 9 to cases with $\zeta/t \neq 0$. Figure 10 shows the neutral curves for the saddles A, B, C and D, and loci where pairs of saddles have the same growth rates. This figure summarizes the qualitatively important features of figures 6, 8 and 9, and extends them. The neutral curves are generated by taking points in figures 6 and 9 where saddles have zero growth rate, and continuing them to non-zero ρ/t and ζ/t respectively while keeping the growth rate zero. The points in figures 6 and 9 where the growth rate curves for the saddles intersect are continued in a similar way and generate the dashed curves. Note that in this figure there is no direct indication of the dominance of the saddles in different parts of the $(\rho/t, \zeta/t)$-plane, nor is there any direct indication of which side of each neutral curve is stable or unstable, but all of this information can be inferred from figures 6, 8 and 9 as follows.

Saddle A is unstable to the right of its neutral curve in figure 10, and is dominant for most of the $\rho/t = 0$ axis (apart from a small interval $-0.00113 < \rho/t < -0.00082$ where C is dominant). If saddle A is followed as ζ/t is increased from zero at a value of ρ/t less than that where the saddle coalescence occurs, e.g. at $\rho/t = 0$, then dominance transfers to B when the first dashed line labelled AB is encountered, and remains with B above that dashed line (as shown in figure 6). However, if saddle A is followed as ζ/t is increased from zero at a value of ρ/t greater than that where the saddle coalescence occurs, e.g. at $\rho/t = 0.0005$, then this saddle remains dominant, though when it reaches the neutral curve attributed to B at the top of figure 10 it has evolved into saddle B (as shown in figure 8). Therefore, whether a saddle is considered to be A or B depends on the path taken in the $(\rho/t, \zeta/t)$-plane, and in particular where that path lies relative to the saddle coalescence point. When we label a saddle, it refers to the saddle on either the $\zeta/t = 0$ axis or $\rho/t = 0$ axis; in the rest of the $(\rho/t, \zeta/t)$-plane the labelling is potentially ambiguous. Saddle B is unstable to the right of its neutral curve, and D is unstable to the left of its neutral curve in figure 10, but D is not dominant.

Having determined the propagation characteristics of an impulsive disturbance for the relatively small propagation velocities near the origin of the $(\rho/t, \zeta/t)$-plane shown in figure 10, we now wish to extend this diagram to include the whole unstable development of the wavepacket. This turns out to be a rather complicated calculation. The main steps are summarized here, and also the final result.† The process corresponds to the development of figure 10 from figures 5, 6, 8 and 9, where saddles are located in complex α-planes, followed as ζ/t and ρ/t are varied, and the loci of neutral saddles, and loci where pairs of saddles have the same heights, are mapped out. The complication arises from the discovery that there are at least nine saddle points in total, and a number of branch points connecting various Riemann surfaces to one another. The arrangement of saddle points on these Riemann surfaces at a particular point in the $(\rho/t, \zeta/t)$-plane is obtained, allowing the dominant saddle to be found at this point. In the example examined in the online supplement this dominant unstable saddle is a quasi-mode. Some of the other saddles are quasi-modes with arrangements of critical points in the complex z-plane like those shown in figures 2(*c*) and 2(*d*). It is not necessary to carry out this analysis of the wavenumber plane at many points in the $(\rho/t, \zeta/t)$-plane. Instead, loci where pairs of saddles have equal heights are mapped out, and changes of dominance examined near these loci, as and when necessary.

Once the dominant saddle is known at any given point in the $(\rho/t, \zeta/t)$-plane, the bounding neutral curve of the disturbance can be computed, as can contours of constant growth rate, and also the frame of reference with strongest growth. The result is shown in figure 11.

This diagram is interpreted as follows: energy is regarded as being essentially generated inside the boundary layer within the frame of reference moving at the velocity of maximum growth rate, i.e. at $\rho/t = 0.1066$, $\zeta/t = 0$, the real group velocity of the disturbance, and which corresponds to the maximum temporal growth rate for real α. Energy then diffuses away from this point of energy generation as this point travels downstream. The flow is absolutely unstable because energy diffuses upstream sufficiently fast for the bounding zero-growth-rate contour to intersect the $\zeta/t = 0$ axis with $\rho/t < 0$. Note also that the energy diffuses away from the energy generation

---

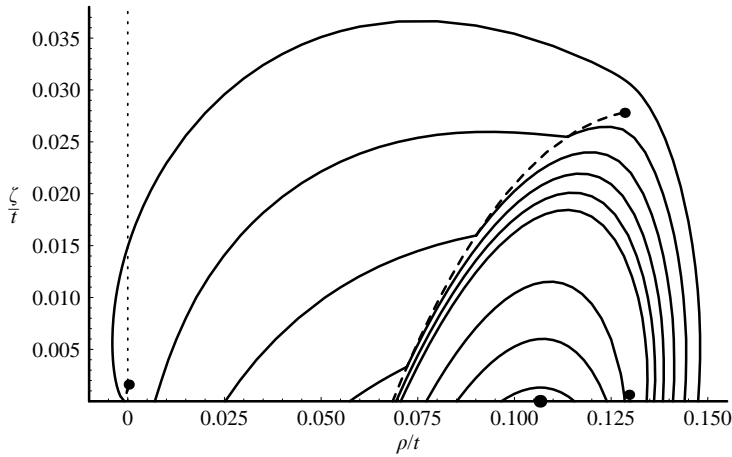† Details are available in an online supplement to this paper.

FIGURE 11. Solid lines are contours of constant growth rates $\mathrm{Re}(\phi_m)$ defined by (4.2) with values 0 (the outer most contour), 0.0002, 0.0004, 0.0006, 0.0008, 0.001, 0.002, 0.003 and 0.004 for $\beta/\rho = 0.007$. The strongest growing part of the disturbance grows at $\mathrm{Re}(\phi_m/Re) = 0.00431$, it travels with velocity components $\rho/t = 0.1066$, $\zeta/t = 0$ and is shown by a black circle. The other circles show saddle coalescence points, and the dashed lines terminating at these points indicate where dominance of the saddles changes.

point in all directions, including out into the free stream, i.e. for $\zeta/t > 0$, and that the amplitude of the disturbance decays monotonically in all directions away from the energy generation point. Nonetheless, the rate of diffusion does depend on the direction from the energy generation point, and does so in such a manner that for certain fixed values of ρ/t, the decay is not monotonic as ζ/t increases. For certain values of ρ/t, including the important rest frame $\rho/t = 0$, there is greater growth at a finite positive ζ/t than at $\zeta/t = 0$.

This non-trivial diffusion of energy into the free stream explains how a disturbance can seemingly propagate and grow indefinitely (at least until the neglected non-parallel effects become important) in the wall-normal direction, even in the absence of basic flow shear outside the boundary layer.

5. Numerical evaluation of an initial-value problem

The prediction of the preceding section that growth can occur in the wall-normal direction in certain frames of reference is surprising, and the method by which this prediction was made, of asymptotic large-time analysis based on saddles with exponentially diverging eigenfunctions, might also seem a little surprising. Therefore, in this section we present an independent solution method applied to a particular initial-value problem based entirely on modes that have exponentially decaying eigenfunctions.

We seek to evaluate (4.1) numerically using an integration path A in the complex wavenumber plane that remains on the Riemann surface that has decaying eigenfunctions for an impulsive disturbance of given azimuthal wavenumber (essentially, we construct the physical wavepacket solution outside the boundary layer from a superposition of normal modes). For comparison with figures 6 and 11, we shall consider $\beta/\rho = 0.007$. The arrangement of the spatial banches for $\rho/t = \zeta/t = 0$ is the same as that in figure 4(d), but we shall not move the branch-cut from the imaginary axis. In principle, the integration path A can be taken along the real α-axis. However,
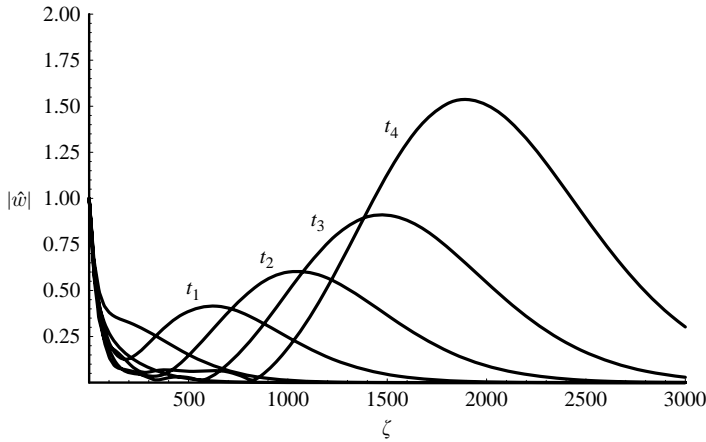
FIGURE 12. Wall-normal disturbance profiles at a succession of times at $\theta = 0$, $\rho = 1$ and $\beta/\rho = 0.007$. The latest times shown are $t_1 = 2 \times 10^5$, $t_2 = 3 \times 10^5$, $t_3 = 4 \times 10^5$ and $t_4 = 5 \times 10^5$. Each profile has been normalized to unit amplitude at $\zeta = 1$, so that they can be compared on the same diagram (the amplitudes increase dramatically with time due to the underlying absolute instability).

the integrand of (4.1) is large and highly oscillatory at large times along that part of the real α-axis where the temporal growth rates are largest. Instead, A has been taken through the dominant saddle via a path that passes along the negative real α-axis up to a small positive real α value, then vertically downwards to the right of the imaginary α-axis to the level of the imaginary part of α at the dominant saddle, horizontally along the steepest descent path through the saddle, then back up to the real α-axis. The resulting path leads to a relatively well-behaved integrand, even though it does not remain entirely within the valleys of the saddle point (it leaves the valley as it passes down the side of the imaginary axis; remaining within the valley would require moving the branch-cut and using exponentially diverging eigenfunctions, which we are choosing to avoid here).

The integral (4.1) is evaluated by first calculating eigenvalues of the dispersion relation for values of α at relatively closely spaced intervals along the path A described above. The quantity Δ_ω is calculated for the same points along A. The eigenvalues ω, and Δ_ω, are then assumed to vary linearly with α between adjacent points on A. At the relatively large numerical values of t and ζ used in these numerical evaluations, the size of the integrand can vary significantly. The total range of integration is divided into the small intervals between successive points along A, and the complete integral is obtained from the sum of all the integrals evaluated between successive points on A. In this way, the size of the integrand does not vary greatly within each integral, making it straightforward to evaluate each integral numerically. Checks on accuracy were carried out by making sure that the result did not depend (within some prescribed tolerance) on the number of points used to divide up the path A, nor on the total length used for A (which obviously could not be taken to $\pm\infty$).

The integral (4.1) has been evaluated for a range of t and ζ for the impulsive boundary forcing (2.10) with $\hat{f}(t) = \delta(t)$. The disturbance envelope, $|\hat{w}(1, 0, \zeta, t)|$, is shown in figure 12. It can be seen that for large enough times the amplitude is indeed larger outside the boundary layer than inside it, and that the wall-normal propagation comes to resemble a growing wavepacket propagating into the free stream. A crude estimate of the group velocity of propagation in the wall-normal direction can be
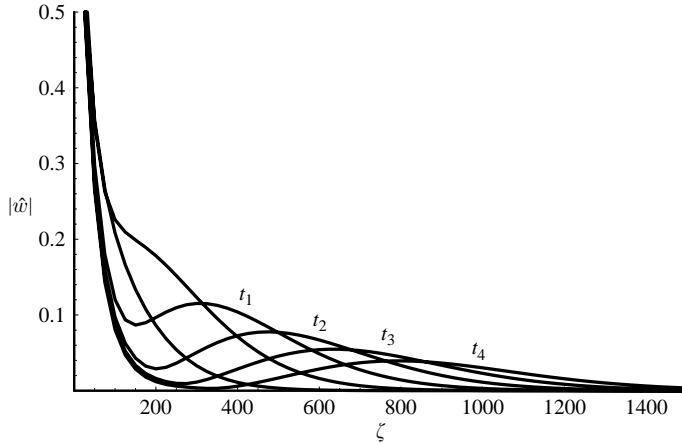
FIGURE 13. Wall-normal disturbance profiles at a succession of times at $\theta = 0$, $\rho = 1$ and $\beta/\rho = 0.01$. The latest times shown are $t_1 = 7.5 \times 10^4$, $t_2 = 10^5$, $t_3 = 1.25 \times 10^5$ and $t_4 = 1.5 \times 10^5$. Each profile has been normalized to unit amplitude at $\zeta = 1$, so that they can be compared on the same diagram (the amplitudes increase dramatically with time due to the underlying absolute instability).

obtained from the graph using the results at t_3 and t_4, giving $\zeta/t \approx 0.005$, which agrees with the result of the saddle-point analysis based on exponentially divergent eigenfunctions (which applies in the limit $t \to \infty$) of $\zeta/t \approx 0.0042$ obtained from the maximum growth rate of figure 6.

   These results justify the removal of the branch-cut from the imaginary axis of the complex α-plane, and the use of saddle points with exponentially diverging eigenfunctions. We can, furthermore, confirm that the appearance of this growth and propagation into the free stream is signalled by spatial branches crossing the imaginary axis of the complex α-plane by repeating the numerical initial-value calculation for $\beta/\rho = 0.01$. At this value of β/ρ the spatial branches do not cross the imaginary axis of the complex α-plane before they pinch with the upstream propagating modes from the lower half-plane (like in figure 4b), meaning that the growth rate will be largest inside the boundary layer, as suggested by figure 7. The results of this numerical integration are shown in figure 13. The growth rate is confirmed to be largest inside the boundary layer, and the decay outside the boundary layer is not monotonic, reflecting the non-monotonic reduction in growth rate with wall-normal propagation velocity predicted by figure 7.

6. Conclusions

   A spatio-temporal analysis of inviscid instability waves in the rotating-disk boundary layer has been carried out. Spatial branches originating in the upper half of the complex radial wavenumber plane are found to cross into the lower half-plane, and then into the left half-plane as the imaginary part of the frequency is reduced for sufficiently small azimuthal wavenumbers. (Or equivalently, the integration path can only be kept within the valley of the dominant saddle by taking it into the left half-plane.) A branch-cut is usually placed along the imaginary axis of the complex radial wavenumber plane to restrict consideration to modes with exponentially decaying eigenfunctions, which automatically satisfy the outer homogeneous boundary condition. Following solutions into the left half-plane requires

moving the branch-cut from the imaginary axis and using modes with exponentially diverging eigenfunctions. Nonetheless, these diverging modes do have a useful physical interpretation in the consideration of the initial-value problem. Certain saddles with diverging eigenfunctions have been shown to describe the wall-normal growth and propagation of disturbances outside the boundary layer.

These divergent saddles have also been used to calculate the disturbance as it propagates in both the streamwise and wall-normal directions, allowing the energy propagation properties to be determined and a description to be provided of how growth can occur in the wall-normal direction in the absence of Reynolds stress terms outside the boundary layer. A somewhat non-trivial diffusion of energy out of the boundary layer and back upstream has been uncovered that sustains the growth seen outside the boundary layer.

All of these predictions based on an asymptotic analysis of saddles with divergent eigenfunctions have been confirmed by an independent solution of the initial-value problem based on numerical evaluation of the inverse Fourier transforms for an impulsive disturbance. This numerical evaluation represents a superposition of modes each with decaying eigenfunctions, yet collectively they generate the growth predicted in the wall-normal direction from the use of saddles with divergent eigenfunctions. The propagation and growth observed in the rest frame $\rho/t = 0$ in figure 12 justifies describing this new phenomenon as a new kind of convective instability. However, it should be recalled that there is an underlying absolute instability in this inviscid calculation, which was scaled out in figures 12 and 13. Healey (2006) shows that there is absolute instability for arbitrarily small β/ρ for inviscid waves, but in principle in the viscous problem there could be decay in the rest frame $\rho/t = \zeta/t = 0$ with growth in frames with $\rho/t = 0$, $\zeta/t > 0$.

The familiar inviscid stability theorems do not apply to these modes with divergent eigenfunctions. The derivations of these theorems rely upon the application of homogeneous boundary conditions, but modes with divergent eigenfunctions do not satisfy homogeneous boundary conditions. Examples have been found that violate Howard's semi-circle theorem where waves with negative phase velocity have been found when the basic velocity profile is non-negative.

It should be emphasized, however, that although saddles with divergent eigenfunctions have been shown to be useful in predicting growth rates and propagation velocities in the wall-normal direction, solutions of the initial-value problem always do satisfy homogeneous boundary conditions.

Inviscid instability waves in the rotating-disk boundary layer have been shown to have maximum growth propagating outside the boundary layer only when the scaled azimuthal wavenumber $\beta/\rho < 0.008424$. The integer azimuthal wavenumber, $n = \beta Re$, must be large for non-parallel effects to be negligible, which suggests that Re will also have to be large, e.g. $Re > 10/(\beta/\rho) > 1200$, before our inviscid calculations are likely to make quantitative predictions. Experiments on the rotating disk at these Re show that the boundary layer is already turbulent. However, the effects of viscosity on the new mechanism are not yet known, and it is possible that qualitatively similar behaviour might be seen at lower Reynolds numbers.

Direct numerical simulations at these Re, like those by Davies & Carpenter (2003), may be feasible, but resolving such a large domain in the z-direction could be problematic. It also seems to be necessary to track the much faster growing downstream convective part of the disurbance, since it is the diffusion of energy from this part of the disturbance out into the free stream, and then back upstream, that sustains the growth in the wall-normal direction. The existence of this kind of energy

transfer mechanism represents an additional challenge in the numerical investigation of global modes.

When streamwise spatial inhomogeneity is included in the basic flow there may be new types of global modes and feedback mechanisms to be identified when the evolution and dyamics outside the shear layer are considered. Although the flow outside the rotating-disk boundary layer is uniform, there may be circumstances where there is weak spatial inhomogeneity in the wall-normal direction as well, opening up the possibility of global modes in this direction too.

The relatively long waves, slow growth rates and slow propagation velocities of the new instability mechanism suggest that it could be further understood by developing an asymptotic long-wave theory. This is indeed the case, see Healey (2005), where the analytic structure of the disturbances, and scalings of various quantities with (β/ρ) are given. The results suggest that growth in the wall-normal direction may even be generic to a wide class of cross-flow instability problems at sufficiently long wavelengths.

It is natural to wonder whether growth in the wall-normal direction might occur in other flows as well. A necessary ingredient is that the flow be unbounded, and uniform, in the direction normal to that of the basic flow, so that eigenfunctions are exponential outside the shear layer. Branch-cuts are then introduced outside the shear layer, and if modes cross these branch-cuts in the manner shown in figure 1(*c*), or figure 4(*d*), then exponential growth outside the shear layer would be found. The addition of viscosity generates additional exponential solutions in the uniform outer flow, with additional branch-cuts, but they do not lie along the imaginary wavenumber axes, see Ashpis & Reshotko (1990). These branch-cuts are further sources of potential growth outside the shear layer. In fact, they represent growth out of viscous layers inside the shear layer, and would generate explosively strong growth compared to the weak growth seen in the inviscid problem because the Reynolds number appears in the exponent. In principle, therefore, there could be growth outside boundary layers (as here), free mixing layers and circular and plane jets and wakes.

Huerre & Monkewitz (1985) found an example of a saddle point crossing the branch-cut in their inviscid spatio-temporal analysis of a free mixing layer, but they did not consider such waves to be physical. Gallaire & Chomaz (2003) also found this behaviour in a study of swirling jets for the axisymmetric mode $n = 0$, and Lim & Redekopp (1998) found this behaviour in variable-density swirling jets. These latter two papers modelled the basic flows with discontinuous and singular functions, and it was argued that the seemingly unphysical divergent eigenfunctions only arose because of their unphysical basic flow models. (For example, the discontinuous Kelvin–Helmholtz profile has arbitrarily large growth rates for small-wavelength disturbances, and represents an ill-posed initial-value problem). These problems would bear further investigation using the methods developed here. It seems that swirling jets can produce growth in the radial direction out into the free stream. One might speculate whether this could be related to the phenomenon of vortex breakdown, or to the 'side-jet' phenomenon found in experiments on heated circular jets by Monkewitz *et al.* (1990), and references therein, in which disturbances are observed to be ejected from the main jet into the surrounding uniform fluid.

However, another family of flows where growth out of a shear layer might be observed at more realistic Reynolds numbers than for the rotating-disk boundary layer considered here, are the flows produced when both the disk and the fluid far from the disk are allowed to rotate with different angular velocities (the fluid far from the disk is in rigid-body rotation). Batchelor (1951) showed that this family of

flows can be described by a similarity solution, which reduces to the von Kármán rotating-disk problem studied here when the fluid has zero angular velocity, reduces to the Ekman (1905) layer when fluid and disk co-rotate at almost the same angular velocity, and reduces to the Bödewadt (1940) layer when the disk is stationary and the fluid rotates. The similarity structure also persists when there is a normal flow through the disk wall, e.g. when there is wall suction, Stuart (1954), or blowing, Kuiken (1971), and also when there is a forced axial flow towards an impermeable disk, see Hannah (1952). Rotating-disk flows of electrically conducting fluids in the presence of magnetic fields have also been calculated, and their stability investigated, see Moresco & Alboussière (2004). Gorla (1992) has calculated the basic flow for a rotating disk driving an electrically conducting fluid subject to a magnetic field with suction at the disk. The methods described in the present paper could be applied directly to all of these flows to investigate the phenomenon of growth out of a boundary layer in a variety of contexts.

REFERENCES

ASHPIS, D. E. & RESHOTKO, E. 1990 The vibrating ribbon problem revisited. *J. Fluid Mech.* **213**, 531–547.

BATCHELOR, G. K. 1951 Note on a class of solutions of the Navier–Stokes equations representing steady rotationally-symmetric flow. *Q. J. Mech. Appl. Maths* **4**, 29–41.

BERS, A. 1983 Space-time evolution of plasma instabilities – absolute and convective. In *Hand-book of Plasma Physics* (ed. M. N. Rosenbluth & R. Z. Sagdeev), vol. 1, pp. 451–517. North-Holland.

BÖDEWADT, U. T. 1940 Die Drehströmung über festem Grunde. *Z. Angew. Math. Mech.* **20**, 241–253.

BRIGGS, R. J. 1964 *Electron-Stream Interaction with Plasmas.* MIT Press.

BRIGGS, R. J., DAUGHERTY, J. D. & LEVY, R. H. 1970 Role of Landau damping in crossed-field electron and inviscid shear flow. *Phys. Fluids* **13**, 421–432.

CHANDRASEKHAR, S. 1961 *Hydrodynamic and Hydromagnetic Stability.* Oxford University Press.

CHESTER, C., FRIEDMAN, B. & URSELL, F. 1957 An extension of the method of steepest descents. *Proc. Camb. Phil. Soc.* **53**, 599–611.

CRIGHTON, D. G. 1989 The 1988 Rayleigh Medal Lecture: Fluid loading – the interaction between sound and vibration. *J. Sound Vib.* **133**, 1–27.

DAVIES, C. & CARPENTER, P. W. 2003 Global behaviour corresponding to the absolute instability of the rotating-disk boundary layer. *J. Fluid Mech.* **486**, 287–329.

DRAZIN, P. G. 2002 *Introduction to Hydrodynamic Stability.* Cambridge University Press.

DRAZIN, P. G. & REID, W. H. 1981 *Hydrodynamic Stability Theory.* Cambridge University Press.

EKMAN, V. W. 1905 On the influence of the earth's rotation on ocean currents. *Ark. Mat. Astr. Fys.* **2**, No. 11.

GALLAIRE, F. & CHOMAZ, J.-M. 2003 Instability mechanisms in swirling flows. *Phys. Fluids* **15**, 2622–2639.

GASTER, M. 1962 A note on the relation between temporally-increasing and spatially-increasing disturbances in hydrodynamic stability. *J. Fluid Mech.* **14**, 222–224.

GASTER, M. 1965 On the generation of spatially growing waves in a boundary layer. *J. Fluid Mech.* **22**, 433–441.

GASTER, M. 1968 Growth of disturbances in both space and time. *Phys. Fluids* **11**, 723–727.

GORLA, R. S. R. 1992 The effects of uniform suction on the magnetohydrodynamic flow over a rotating disk. *Intl J. Engng Fluid Mech.* **5**, 413–433.

GREGORY, N., STUART, J. T. & WALKER, W. S. 1955 On the stability of three-dimensional boundary layers with application to the flow due to a rotating disk. *Phil. Trans. R. Soc. Lond.* A **248**, 155–199.

HANNAH, D. M. 1952 Forced flow against a rotating disc. *ARC-RM* -2772.

HEALEY, J. J. 1995 On the neutral curve of the flat-plate boundary layer: comparison between experiment, Orr–Sommerfeld theory and asymptotic theory. *J. Fluid Mech.* **288**, 59–73.

HEALEY, J. J. 1998 Characterizing boundary-layer instability at finite Reynolds numbers. *Eur. J. Mech.* B/*Fluids* **17**, 219–237.

HEALEY, J. J. 2004 On the relation between the viscous and inviscid absolute instabilities of the rotating-disk boundary layer. *J. Fluid Mech.* **511**, 179–199.

HEALEY, J. J. 2005 Long-wave theory for a new convective instability with exponential growth normal to the wall. *Phil. Trans. R. Soc. Lond.* A **363**, 1119–1130.

HEALEY, J. J. 2006 Inviscid long-wave theory for the absolute instability of the rotating-disk boundary layer. *Proc. R. Soc. Lond.* A. **462**, 1467–1492.

HINCH, E. J. 1991 *Perturbation Methods.* Cambridge University Press.

HOWARD, L. N. 1961 Note on a paper of John W. Miles. *J. Fluid Mech.* **10**, 509–512.

HUERRE, P. & MONKEWITZ, P. A. 1985 Absolute and convective instabilities in free shear layers. *J. Fluid Mech.* **159**, 151–168.

KÁRMÁN, TH. VON 1921 Über laminare und turbulente Reibung. *Z. Angew. Math. Mech.* **1**, 233–252.

KUIKEN, H. K. 1971 The effect of normal blowing on the flow near a rotating disk of infinite extent. *J. Fluid Mech.* **47**, 789–798.

LIM, D. & REDEKOPP, L. 1998 Absolute instability conditions for variable density, swirling jet flows. *Eur. J. Mech.* B/*Fluids* **17**, 165–185.

LIN, C. C. 1955 *Hydrodynamic Stability Theory.* Cambridge University Press.

LINGWOOD, R. J. 1995 Absolute instability of the boundary layer on a rotating disk. *J. Fluid Mech.* **299**, 17–33.

MONKEWITZ, P. A., BECHERT, D. W., BARSIKOW, B. & LEHMANN, B. 1990 Self-excited oscillations and mixing in a heated round jet. *J. Fluid Mech.* **213**, 611–639.

MORESCO, P. & ALBOUSSIÈRE, T. 2004 Stability of Bödewadt–Hartman layers. *Eur. J. Mech.* B/*Fluids* **23**, 851–859.

SCHMID, P. J. & HENNINGSON, D. S. 2001 *Stability and Transition in Shear Flows.* Springer.

SHRIRA, V. I. & SAZONOV, I. A. 2001 Quasi-modes in boundary-layer-type flows. Part 1. Inviscid two-dimensional spatially harmonic perturbations. *J. Fluid Mech.* **446**, 133–171.

STUART, J. T. 1954 On the effects of uniform suction on the steady flow due to a rotating disk. *Q. J. Mech. Appl. Maths.* **7**, 446–457.

TURKYILMAZOGLU, M. & GAJJAR, J. S. B. 2001 An analytic approach for calculating absolutely unstable inviscid modes of the boundary layer on a rotating disk. *Stud. Appl. Maths.* **106**, 419–435.

WONG, R. 1989 *Asymptotic Approximations of Integrals.* Academic.